Time-Resolved Femtosecond Stimulated Raman Spectra and DFT Anharmonic Vibrational Analysis of an Electronically Excited Rhenium Photosensitizer

Journal:	*The Journal of Physical Chemistry*
Manuscript ID	jp-2019-10840r.R2
Manuscript Type:	Article
Date Submitted by the Author:	n/a
Complete List of Authors:	Pizl, Martin; Ustav fyzikalni chemie J Heyrovskeho Akademie Ved Ceske Republiky, Picchiotti, Alessandra; Institute of Physics Czech Academy of Sciences Rebarz, Mateusz; Institute of Physics Czech Academy of Sciences Lenngren, Nils; Institute of Physics Czech Academy of Sciences Yingliang, Liu; Institute of Biotechnology Czech Academy of Sciences Zalis, Stanislav; Ustav fyzikalni chemie J Heyrovskeho Akademie Ved Ceske Republiky, Kloz, Miroslav; Institute of Physics Czech Academy of Sciences Vlcek, Antonin; Queen Mary University of London, SBCS

Time-Resolved Femtosecond Stimulated Raman Spectra and DFT Anharmonic Vibrational Analysis of an Electronically Excited Rhenium Photosensitizer

Martin Pižl,[a,b] Alessandra Picchiotti,[c] Mateusz Rebarz,[c] Nils Lenngren,[c] Liu Yingliang,[d] Stanislav Záliš,[a] Miroslav Kloz,*[,c] Antonín Vlček*[,a,e]

[a] J. Heyrovský Institute of Physical Chemistry, Czech Academy of Sciences, Dolejškova 3, 182 23 Prague, Czech Republic
[b] Department of Inorganic Chemistry, University of Chemistry and Technology, Prague, Technická 5, CZ-166 28 Prague, Czech Republic
[c] ELI Beamlines, Institute of Physics, Czech Academy of Sciences, Na Slovance 1999/2, 182 00 Prague, Czech Republic
[d] Institute of Biotechnology, Czech Academy of Sciences, Průmyslová 595 252 50 Vestec, Czech Republic
[e] Queen Mary University of London, School of Biological and Chemical Sciences, Mile End Road, London E1 4NS, United Kingdom

Abstract

Time-resolved femtosecond stimulated Raman spectra (FSRS) of a prototypical organometallic photosensitizer/photocatalyst $ReCl(CO)_3$(2,2'-bipyridine) were measured in a broad spectral range ~40–2000 (4000) cm^{-1} at time delays from 40 fs to 4 ns after 400 nm excitation of the lowest allowed electronic transition. Theoretical ground- and excited-state Raman spectra were obtained by anharmonic vibrational analysis using second-order vibrational perturbation theory on vibrations calculated by harmonic approximation at DFT-optimized structures. A good match with anharmonically calculated vibrational frequencies allowed for assigning experimental Raman features to particular vibrations. Observed frequency shifts upon excitation (ν(ReCl) and ν(CC inter-ring) vibrations upwards; ν(CC, CN) and ν(Re-C) downwards) are consistent with the bonding/antibonding characters of HOMO and LUMO involved in the excitation and support the delocalized formulation of the lowest triplet state as $ReCl(CO)_3 \rightarrow$bpy charge-transfer. FSRS

spectra show a mode-specific temporal evolution, providing insight into the intersystem crossing (ISC) mechanism and subsequent relaxation. Most of the Raman features are present at ~40 fs and exhibit small shifts and intensity changes with time. The 1450–1600 cm^{-1} group of bands due to CC, CN, and CC(inter-ring) stretching vibrations undergoes extensive restructuring between 40 and ~150 fs, followed by frequency upshifts and a biexponential (0.38, 21 ps) area growth, indicating progressing charge separation in the course of the formation and relaxation of the lowest triplet state. Early (40–150 fs) restructuring was also observed in the low-frequency range for ν(Re-Cl) and δ(Re-C-O) vibrations that are presumably activated by ISC. FSRS experimental innovations employed to measure low- and high- energy Raman features simultaneously are described and discussed in detail.

■ INTRODUCTION

Time-resolved vibrational spectroscopic methods are excellent techniques to characterize electronically excited states, as well as products and intermediates of photochemical reactions. Time-resolved infrared (TRIR)[1,2] and Raman[3,4,5,6,7] experiments provide structural and dynamical information through temporal evolution of spectral patterns, band shapes, and intensities. Comparing ground- and excited-state spectra allow us to understand structural changes and electron-density redistribution upon excitation. The time evolution of IR and Raman band positions and shapes report on relaxation processes while time-dependent band intensities (areas) shed light on excited-state decay and reactivity.

To extract maximum information from vibrational spectroscopic experiments, we need to measure over spectral and temporal ranges as broad as possible and the spectral features

must be correctly assigned to corresponding vibrations. TRIR spectra are usually reported at frequencies higher than ~1100 cm^{-1}, often focusing on strong IR chromophores (inorganic carbonyls, cyanides, isocyanides, SCN-, -C≡C-, etc.) that give rise to well-separated bands between 1800 and 2300 cm^{-1}. Important results were also obtained in the region aromatic CC vibrations[2] which, however, is more crowded, complicating the spectral assignment. Time-resolved femtosecond stimulated Raman spectroscopy (TR-FSRS) is complementary to TRIR and could be more selective for particular chromophores owing to (pre)resonance enhancement. Although the low-frequency range (~40–800 cm^{-1}) could be very informative, most FSRS studies report spectra above ~800 cm^{-1}, presumably due to technical difficulties in generating the probing white-light continuum close to the Raman pump wavelength.

Assignment of intense high-frequency vibrational bands can be done empirically in combination with symmetry arguments, but this approach often fails in fingerprint and, especially, low-frequency regions. Moreover, molecular vibrations are substantially more delocalized over different bonds and more strongly coupled than can be captured by empirical assignments. Contemporary DFT software packages routinely perform vibrational analysis by treating molecular vibrations as harmonic oscillators. Such calculations predict main spectral features and corresponding normal coordinates. However, the quantitative match between calculated and experimental frequencies often is not satisfactory, with accuracy decreasing at lower frequencies. Multiplicative correction factors, which depend on the basis set and the functional, are often used. The harmonic approximation misses overtones and combination bands that contribute to spectral patterns and affect band shapes. It predicts equal energy spacing between vibrational levels and neglects many vibrational couplings, and is thus

unsuitable for interpretation of diagonal and off-diagonal anharmonicities and cross-peaks in 2-dimensional IR spectra.[8,9] Anharmonic vibrational calculations overcome these problems. Computational techniques based on second-order vibrational perturbation theory (VPT2) suitable for medium-size molecular systems have been implemented only recently and were found to considerably improve the match between theory and experiment and to enable assignments of elusive spectral features.[10,11,12,13,14]

We report time-resolved FSRS of ground- and lowest electronic excited states of *fac*-$ReCl(CO)_3(bpy)$ (bpy = 2,2'-bipyridine) measured across the full chemically relevant range (100–4000 cm^{-1}), together with their anharmonic DFT assignments. $ReCl(CO)_3(bpy)$ is a prototypical member of the rhenium-carbonyl-polypyridine family of versatile redox photosensitizers/photooxidants and luminescent imaging agents.[15,16,17] It also is a well-known photo- and electro-catalyst of CO_2 reduction.[18,19,20,21] In most cases, TRIR is the technique of choice to study excited states of $ReCl(CO)_3(bpy)$ and its congeners, owing to the presence of strong $\nu(C{\equiv}O)$ IR bands that are highly sensitive to the electron density distribution.[1,15,22,23,24,25] In particular, the lowest excited state of $ReCl(CO)_3(bpy)$ was unambiguously characterized by $\nu(CO)$ TRIR spectra as predominantly metal-to-ligand charge transfer (MLCT) and approximately formulated as $Re^{II}Cl(CO)_3(bpy^{\bullet-})$.[14,15,22,23,26] High-frequency IR features of both the electronic ground and excited states were assigned by anharmonic DFT calculations, which also identified bpy-based combination bands occurring unexpectedly close to $\nu(CO)$ features.[14] Far less is known about the behavior of bpy-localized and low-frequency skeletal modes whose IR signatures are much weaker or wholly unavailable. Some of the excited-state bpy-localized vibrational features were observed in the static transient resonance Raman (TR^2) spectrum of

$ReCl(CO)_3(bpy)$ measured with a 364 nm pump,[27] while picosecond temporal evolution of several bpy-localized Raman bands of $ReCl(CO)_3(bpy)$ and $[Re(4\text{-Et-pyridine})(CO)_3(bpy)]^+$ was followed by time-resolved resonance Raman spectra (TR^3) probed at 400 nm.[26] Both experiments took advantage of (pre)resonance enhancement due to a strong $\pi\pi^*(bpy^{\bullet-})$ electronic transition at 373 nm

This study demonstrates the power of combining TR-FSRS experiments in the range of skeletal and ligand-localized vibrations with DFT calculations and 2nd order perturbational anharmonic DFT vibrational analysis in characterizing structural and electronic changes upon excitation and excited-state evolution on the femto-picosecond timescale.

■ EXPERIMENTAL AND COMPUTATIONAL TECHNIQUES

Materials

$ReCl(CO)_3(bpy)$ was prepared according to a literature procedure[28] by a ~3hr reflux of $Re(CO)_5Cl$ and 2,2'-bpy in a 1:1.1 molar ratio (both Sigma-Aldrich) in degassed toluene followed by extensive washing of the precipitated product with toluene and diethylether. Purity was checked by IR and NMR. Nearly saturated solutions in CH_3CN and CD_3CN (Sigma-Aldrich, spectroscopic quality) were used under air atmosphere.

Femtosecond Stimulated Raman Spectroscopy

The FSRS setup at ELI-Beamlines (Inst. of Physics, Prague) is pumped by a commercial 1 kHz titanium sapphire femtosecond amplifier system Femtopower (Spectra-Physics) generating 20 fs pulses centered at 800 nm. The beam is split by dielectric beam splitters into three

synchronized beam paths: 1 mJ driving the “actinic pump” generation, 1.5 mJ driving the “Raman pump” generation, and 200 μJ driving the “probe” generation. Actinic pulses are converted to 400 nm by second-harmonic generation in a BBO crystal and passed through an optical delay line that allows setting their timing relative to probe and Raman pump pulses with a sub-10 fs precision. Actinic pulses are attenuated to an average energy of 2 μJ at the sample by a gradient neutral-density filter. Raman pump pulses are generated by sending 800 nm, ~20 fs driving pulses through a home-built 4f pulse shaper that selects a spectrally narrow interval, effectively generating pulses approximately 1 nm broad, 2 ps long, and with ~3 μJ energy, whose center wavelength is tunable within the ~1000 cm^{-1} width of the generating 800 nm pulse. A chopper wheel[29] installed in the Fourier plane of the pulse shaper consecutively generated 96 different wavelengths of the Raman pump pulse, each shifted by approximately 10 cm^{-1} from the previous one in the 765–835 nm interval. Pulses were adjusted to an average energy of 3 μJ at the sample by a linear-gradient neutral density filter. The probe is generated by a two-stage process. A home-built supercontinuum-seeded NOPA converts 800-nm pulses into 1400-nm pulses that are subsequently focused into a 2-mm sapphire plate, generating the probe supercontinuum, which is separated from the 1400 nm driving pulses by a dichroic beamsplitter. The probe supercontinuum spectrum spans from 350 to 1200 nm and is conveniently flat around the 800 nm Raman pump wavelength. The relative polarization of Raman pump and probe beams were set parallel by a half-wave-plate in the Raman pump path, while polarization of the actinic pulse was set to the magic angle (54.7°) relative to the probe using a half-wave-plate, in order to suppress possible polarization-related effects. The relative

timing of Raman pump and probe pulses is adjusted to provide maximal FSRS signal, which is known to occur close to, but not exactly at, the perfect temporal overlap.[30]

After the sample, the probe is split into two copies that are spectrally imaged and analyzed by two respective imaging spectrographs (Acton Princeton Instruments) operating in 0-2000 and 2000-4000 cm^{-1} ranges. Each spectrograph is equipped with a FFT CCD 1024 x 58 pixel array camera operating at 1 kHz at full vertical binning, effectively working as a linear sensor (Entwicklungsbuero Stresing). Both cameras are read simultaneously for each shot, together with a photodiode signal that records the Raman pump pulse energy. This photodiode signal is used for synchronization and parallel detection of the 96 individual FSRS experiments (each obtained with a differently shifted Raman pump wavelength) in 100 ms cycles, where 96 ms is used for recording FSRS and 4 ms for recording transient absorption. This is a compromise between the duration of the experiment and the signal intensity since Raman signals are usually considerably weaker than transient absorption signals, which therefore require shorter acquisition time. The 96 individually shifted Raman signals are recombined into a single spectrum with a highly suppressed baseline and pixelation artifacts by the "watermarking" approach described elsewhere.[29] Each time-delay point is a result of a 1 minute accumulation time.

For each time delay, a ground- and excited-state Raman, and TA signals are measured. This is achieved by chopping the actinic pump at 500 Hz. To record both ground- and excited-state Raman signals for each position of the modulator, the phase of the chopper inserted in the actinic beam path is flipped by 180° at regular intervals. This “phase flip” approach cancels out any artifacts related to irregularities in the Raman pulse modulator shape.[29,31] Each of the

two CCD array cameras records a spectral interval approximately 2000 cm^{-1} wide, covering the 0–2000 cm^{-1} and 2000–4000 cm^{-1} ranges, respectively. The signals are numerically stitched together, so the entire 0–4000 cm^{-1} range is observed simultaneously. Detectors are calibrated by recording FSRS of a 1:1 (v:v) toluene:acetonitrile mixture with accurately known Raman spectrum.[32]

In present experiments, the probe beam was focused to a spot of ~40 μm diameter at the sample and overlapped with ~100 μm Raman and actinic pump beams. The delay of the actinic pump was scanned from 200 ps before to 6 ns after the arrival of the FSRS probe in 134 logarithmically distributed delay times, providing approximately 8 time points for each doubling of the delay time. Each experiment was repeated several times to verify reproducibility and, for each data point, a median value was selected for analysis. Sample solutions were flowed in a 10x1x1 mm rectangular quartz flow cell (custom-made by Firefly Sci, Inc.). The flow speed was set to ensure a fresh sample spot for each laser shot with a peristaltic pump (mzr-4622-hs-f from HNP Mikrosysteme GmBH). Minimal sample damage (below 1%) was verified by measuring absorption spectra before and after the experiment in a conventional 1 mm quartz cell (Hellma) in a commercial spectrometer (2800 Shimadzu).

Residual baselines in the data were corrected by fitting 9^{th} order polynomials using the method of least absolute value residuals. In comparison to the least-square fitting, the baseline obtained by this method is less sensitive to sharp changes, for example at bases of narrow peaks. (The least-square procedure by definition fits into the center of the data and thus the baseline does not follow the pedestals of the peaks but goes through their centers. Corrected signals then tend to have a Mexican hat shape. This problem does not occur with least absolute

residual fitting where polynomial fitting removes the broadband baseline from narrowband peaks at their bases.)

Ground-state FSRS spectra labeled "Exp" and "Exp2" are based on the same raw data but differently analyzed: "Exp" shows data processed by spectral watermarking,[29] while "Exp 2" spectra were obtained by averaging of shifted signals that were numerically aligned according to their Raman shift. The latter approach produces a spectrum that is very close to the raw single-wavelength FSRS but with an improved fixed-pattern noise as the shifted spectra are recorded at varied positions of the detector. In general, watermarking produces a superior baseline that is, however, prone to specific artifacts when the Raman pulse at 0 cm^{-1} is scattered within the watermark. Hence, there are only small differences at higher wavenumbers, whereas a notable difference occurs below 400 cm^{-1}. In general, this work shows that measuring very small Raman shifts with FSRS is possible but extra care is required when spectral modulation is applied since peak shapes can change as individual shifted FSRS measurements are in a different state of resonance.[33] It follows that spectral watermarking will require specific corrections when applied closer to resonance.

Measuring FSRS at low wavenumbers and over broad spectral ranges

To measure FSRS over a broad wavenumber range, a 2-stage probe preparation was used, whereby the probe is generated from a driving beam whose wavelength is beyond the sensitivity range of the silicon detector. This approach has two key advantages for the FSRS experiment: It allows generating probe pulses that have a flat spectral profile in the 450–1100 nm interval (or, 350–1100 when CaF_2 is used instead of sapphire) and, at the same time,

exponentially increasing intensity between 1100 and 1200 nm, thus compensating for an exponential loss of the silicon-detector sensitivity in this range. Note that the spectral intensity of a single-filament supercontinuum drops very rapidly upon moving from the generating wavelength and a relatively flat spectral profile is reached only at a substantial distance. Thus, FSRS experiments where the Raman pump and the probe-supercontinuum generating pulses are centered at the same wavelength (often at 800 nm for Titanium Sapphire lasers) operate in a truncated detection range, as small Raman shifts suffer from an excessive probe intensity, while highly Raman-shifted peaks suffer from a weak probe intensity. Such experiments have narrow effective spectral ranges, with only a few Raman signals in the detection optimum. In contrast, our experimental setting allows recording vibrations in the 40–4000 cm^{-1} range simultaneously with excellent homogeneous sensitivity. (Performance in the low-end of this range is demonstrated in Figure S9.) This approach is superior to single-stage probe generation either by a single NOPA[34] or by a single supercontinuum process.[35] Spectra at low wavenumbers can also be recorded by impulsive stimulated Raman experiments performed in the time domain,[36,37] however this approach struggles with recording high-energy vibrations since few-cycle pulses as short as 5 fs are required for exciting vibrations at wavenumbers above 2000 cm^{-1}. Moreover, impulsive Raman spectra have to be corrected for the temporal pulse envelope and thus produce patterns that often differ substantially from those recorded by spontaneous Raman scattering. Furthermore, the time-domain approach needs scanning to record spectra and is therefore sensitive to laser instability. In contrast, the FSRS approach used herein allows for simultaneous observation of both low- and high-energy vibrations with a good agreement with spontaneous Raman spectra for each shot. Typically, few thousands shots are

averaged to achieve a good signal-to-noise ratio, but this process is independent of the short-term laser instability.

Computational details

Calculations were performed using Gaussian 16, Revision A.03 (G16)[38] together with the three-parametrized Becke, Lee, Yang, Park (B3LYP) functional.[39,40] For the Re atom, we used a large basis set (8s7p6d2f1g)/[6s5p3d2f1g] and a standard Stuttgart/Dresden pseudopotential for 60 core electrons.[41,42] For non-metal atoms we used the 6-31+G(d) basis set.[43] Solvent effects (acetonitrile) were described by the polarizable continuum model (PCM).[44] The lowest triplet excited state was calculated by the unrestricted Kohn-Sham approach (UKS). Calculations started from a previously optimized structure[14] that was reoptimized with G16 and PCM-CH_3CN. Triplet–triplet electronic excitations were calculated by time–dependent DFT approach at UKS-optimized geometry.

Anharmonic calculations were based on the second-order vibrational perturbation theory (VPT2) model,[11,13,45,46,47] which provides an accurate description of anharmonic vibrational energies and wave functions. Fermi and Darling-Dennison resonances were treated by the generalized VPT2 procedure[48] (GVPT2) on calculated anharmonic potential energy surfaces obtained by the deperturbed VPT2 scheme (DVPT2). Cubic and semidiagonal quartic force constants were computed by numerical differentiation (with displacements of 0.01 Å) of the analytical Hessian along each active normal coordinate. In the first step, a full dimensionality (FD) calculation included all vibrational modes. Afterwards, large-amplitude motions (LAMs) were identified and their contributions were skipped from GVPT2 calculations.

Out of the 78 vibrational modes of $ReCl(CO)_3(bpy)$ 53 and 62 modes were active in calculations of GS and ES spectra, respectively. The VMS-Draw[49] graphical user interface was used to analyze the outcome of vibrational computations.

■ RESULTS

Time-resolved FSRS of $ReCl(CO)_3(bpy)$ were measured in CH_3CN and CD_3CN solutions upon 400 nm, 40 fs excitation into the lowest MLCT absorption band. The 800 nm Raman pump pulse (2 ps, 16 cm^{-1} fwhm) is out-of-resonance for the ground state whose lowest allowed electronic absorption band occurs at 371 nm.[28,50] On the other hand, the Raman pump falls into the weak/broad absorption of the lowest ^{3}MLCT excited state that originates from $\pi\pi^*$ transitions localized at the $bpy^{\bullet-}$ ligand (Figure S1).[51,52] The broad-band white-light continuum (Raman probe) was generated using pulses at a wavelength (1400 nm) longer than that of the Raman pump in order to achieve a relatively smooth/flat profile in the 800–1200 nm interval where the Raman signals occur, thus enabling to measure spectra at small Raman shifts values, from ca. 40 cm^{-1}. Additionally, we used watermarking,[29] whereby multiple experiments with slightly shifted Raman wavelengths are performed in parallel and recombined into a single Raman spectrum with a greatly improved baseline and decreased fixed-pattern noise. These two technical innovations allowed us to obtain good-quality spectra over a very broad spectral range.

Ground- and excited-state Raman spectra and their assignment

Ground-state FSRS of $ReCl(CO)_3(bpy)$ spectra are shown in Figures 1 and S2, together with those calculated using harmonic and anharmonic approximations. The peak wavenumbers are summarized in Table 1 and selected vibrational modes are visualized in Chart S1. Anharmonically calculated wavenumbers and the overall spectral pattern match well the experimental spectrum, except for the ν(CO) vibrations whose wavenumbers were calculated accurately (as compared with IR values[14]) but the theoretical Raman intensities are much higher than the weak signals apparent in CH_3CN (Figure S2). A strong band belonging to bpy-ring CC and CN stretching vibrations occur at 1600–1605 cm^{-1} whereas the predominantly inter-ring ν(CC) band is observed at 1490–1493 cm^{-1}. Inter-ring stretching contributes to several other modes as well, especially to the intense feature at 1314–1319 cm^{-1}. Re-CO stretching vibrations are observed at ~479 and 500–507 cm^{-1}, usually coupled with ReCO deformations. The Re-Cl stretch makes the principal contribution to the 239–243 cm^{-1} feature, while also contributing to the modes at 256–265 and 115 cm^{-1}, where it is usually coupled with deformations of the Re(bpy) moiety. Few bands deviate from the anharmonically calculated spectrum. Namely, the calculation overestimates vibrational wavenumbers in the 1550-1650 cm^{-1} range. The feature observed at 1568 (CH_3CN) and 1557 cm^{-1} (CD_3CN) was thus tentatively attributed to the ν(CN, CC) mode 64 calculated at 1600 cm^{-1}, with a possible contribution from a 52+20 combination band calculated at 1581 cm^{-1}. The strong band at 1600-1605 cm^{-1} most likely encompasses ν(CN, CC) modes 66 and 67 calculated at 1622 and 1633 cm^{-1}, respectively. Features at 1368 (possibly solvent) and 915 cm^{-1} also do not match any calculated strong Raman band and their assignment (Table 1) remains tentative.

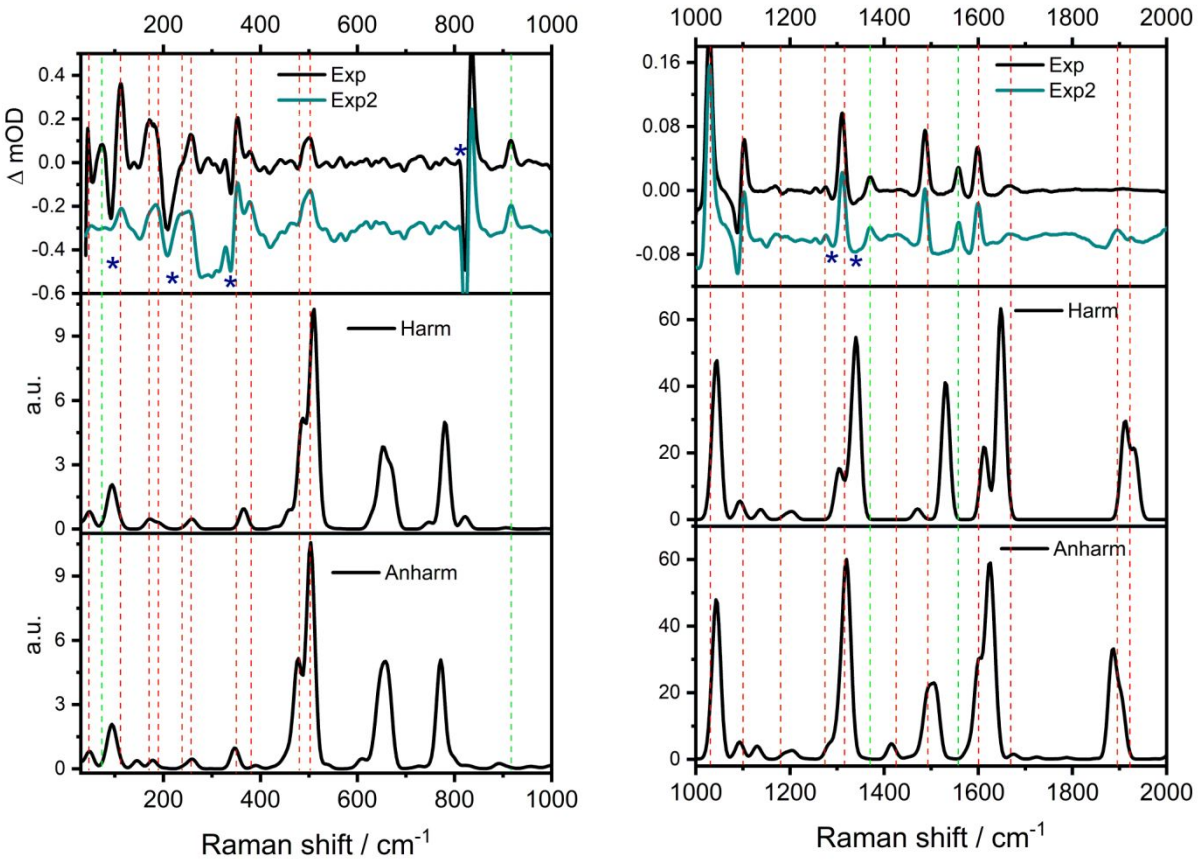

Figure 1. Ground-state FSRS of $ReCl(CO)_3(bpy)$ in CD_3CN (top), together with harmonically (middle) and anharmonically (bottom) calculated Raman spectra. Exp and Exp2 spectra in the top panel originated from the same raw data that were analyzed using "watermarking" and averaging of shifted signals, respectively. (See the Experimental section.) Red vertical lines connect experimental and corresponding anharmonically (bottom) calculated Raman features. Green vertical lines show experimental Raman bands without obvious calculated counterparts. * denotes residual solvent features and background artifacts. a.u. = arbitrary units. No significant spectral features were observed between 2000 and 4000 cm^{-1}. Spectra measured in CH_3CN are shown in Figure S2.

Table 1. Experimental[a] and calculated Raman spectra of ground-state $ReCl(CO)_3(bpy)$.

# [b]	Principal vibrations [c]	Experimental	Harmonic	Anharmonic	Relative int. [c]
70	$\nu(CO)$	2021	2054	2024	20.5
69	$\nu(CO)_{asym,eq}$	1916	1932	1904	33
68	$\nu(CO)_{ax} + \nu(CO)_{sym,eq}$	1894	1911	1884	59.6
	58+17	1666	-	1675	3.2
67	ν(CN, CC)	1605 (1600)	1655	1633	40.8
66	$\nu(CC)_{ring}$		1647	1622*	78.2
64	ν(CN, CC)	1568 (1557)	1612	1600*	55.9
	52 +20		-	1581	4.4
63	ν(CC inter-ring, CC) + δ(CH)	1493 (1490)	1531	1510*	39.7
	58 +12		-	1493	34.4
	40 + 28	(1425)	-	1426	0.8
60	ν(CN, CC, CC-inter-ring)	1410 ?	1471	1415*	8.4
59	ν(CC) + δ(bpy, CH)	(1368)	1351	1351	1.2
58	ν(CC inter-ring, CN) + δ(CH)	1319 (1314)	1340	1319*	100
55	ν(CN), δ(CH)	(1275)	1299	1283	8.6
53	δ(CH)	(~1181) ?	1191	1188	3.4
52	δ(CH)	-	1152	1135	1.2
49	ν(CC), δ(CH)	(1100)	1093	1093*	10.5
47	$\delta(bpy)_{sym}$-breath + δRebpy	1033 (1030)	1044	1044*	91.9
46	$\delta(bpy)_{antisym}$-breath + δRebpy		1034	1034*	12.4
	28 + 21	(970)	-	975	0.002
41	$\delta(CH)_{sym,\ out\text{-}plane}$	(915)	909	909	0.1
	20 overtone		-	893	0.3
40	$\delta(CH)_{antisym,\ out\text{-}plane}$		901	886	0.2
38	$\delta(bpy)_{sym}$-breath	767 ?	781	771	10.2
35	$\delta(CH)_{sym}$ + ν(CC inter-ring)	-	745	727	0.2
32	ν(ReN), δ(CC)	-	652	649	6.3
30	δ(Re-C-O)	-	632	607	0.8
28	$\delta(CC, CH)_{antisym,\ out\text{-}plane}$	-	563	537	0.2
25	$\nu(Re\text{-}CO)_{ax}$ $\delta(Re\text{-}C\text{-}O)_{eq}$	507 (500)	510	504*	20.5
23	$\nu(Re\text{-}CO)_{eq}$ $\delta(Re\text{-}C\text{-}O)_{ax}$	(479)	486	478*	5.9
	-	432	-	-	
21	δ(CC)+ δ(Rebpy)	-	460	456	1.4
20	$\delta(CC, CH)_{antisym,\ out\text{-}plane}$ δ(O-C-Re)	-	456	442	0.4
18	$\delta\ (CC, CH)_{sym,\ out\text{-}plane}$	(380)	430	390	0.3
17	$\delta(bpy)_{out\text{-}plane}$	(352)	365	347*	1.9
	-	311 (307)	-	-	

	-	(290)	-	-	
16	$\delta(bpy)_{out\text{-}plane} + \nu(ReCl)$	265 (256)	261	261*	0.4
15	$\delta(bpy)_{out\text{-}plane} + \nu(ReCl)$		259	259*	0.5
14	$\nu(ReCl) + \delta(Rebpy)$	243 (239)	248	244*	0.3
12	$\delta(bpy)_{sym,\ out\text{-}plane} + \delta(Rebpy)$	(189) 177 (170)	190	178*	0.8
10	$\delta(bpy)_{antisym,\ out\text{-}plane} + \delta(ReCl)$	(115)	107	107	0.6
9	$\delta(ReCl) + \delta(bpy) + \delta(ReCO)$		100	100	0.5
8	$\delta(bpy) + \delta(CO)$	-	95	95	1.1
7	$\delta(CO) + \delta(ReCl)$		94	94	1.4
6	$\delta(ReCO) + \delta(CReCl) + \delta(bpy)$		92	92	1
2	$\delta(bpy) + \delta(ReCO) + \delta(ReCl)$	(45) ?	48	48	1.7

[a] Data from CH_3CN or (CD_3CN) solutions. No significant spectral features were observed between 2000 and 4000 cm^{-1}. ? after an experimental wavenumber indicates a weak or uncertain feature. [b] Normal mode number in the order of increasing frequency. [c] Based on anharmonic calculation. Deformations of the Rebpy moiety (δ(Rebpy)) involve ReN stretches. * Vibration shown in Chart S1.

Excited-state FSRS measured at 60 ps when the ^{3}MLCT state is thermalized[25,26,53,54] is compared with theoretical spectra in Figures 2, S3. Anharmonic vibrational analysis of the UKS-DFT optimized lowest ^{3}MLCT excited state identified excited-state Raman features and characterized the corresponding vibrations (Table 2, Chart S2). A good match between calculated and experimental frequencies was obtained while the intensity patterns are not directly comparable since experimental intensities are partly affected by resonance with $\pi\pi^*(bpy^{\bullet-})$ transitions (Figure S1). Thus, the most intense calculated Raman band due to the totally symmetric in-phase ν(CO) vibration is not observed in the experimental spectrum whereas $bpy^{\bullet-}$ - vibrations and some of the low-frequency modes give rise to well-developed signals. Calculations also provided the Duschinsky matrix (Figures 3, S4) that correlates ground- and excited-state vibrations. The matrix shows considerable remixing among CC and CN stretching and CH bending modes of the bpy ligand (55-67) on going to the excited state. For

example, the excited-state mode 67 contains 22 % and 65 % contributions of ground-state ν(CC, CN) modes 65 and 67, respectively. The predominantly inter-ring CC stretch ground-state mode 58 at 1314–1319 cm^{-1} contributes to excited-state vibrations 57 (26%, at ~1278 cm^{-1}) and 59 (61%, at 1370 cm^{-1}) and to a host of higher-lying modes. Remixing also occurs between δ(bpy)/δ(CH)/δ(Rebpy) modes 40–53, deformation and Re-CO stretching vibrations 20-30, the group of related ν(ReCl)/δ(Rebpy) vibrations 14–16, as well as among low-frequency modes 1–10.

Excited-state FSRS shows strong ν(CC, CN) and ν(CC-ring, inter-ring) features at ~1550 and ~1500 cm^{-1}, respectively. The inter-ring CC stretch contributes to vibrations 64, 63, 60, and 59 that occur in the range 1370–1500 cm^{-1}. However, the only modes well visible in the spectrum are 64 (1502 cm^{-1}) and 60 (~1420 cm^{-1}). The band due to the principal ν(CC inter-ring) mode 59 (1370 cm^{-1}) is barely apparent, in contrast to the corresponding strong GS feature 58 at 1314–1319 cm^{-1}. On the other hand, the excited-state spectrum shows bands at ~1174 (δ(CH)), 1217 (δ(CH)), and ~1278 (ν(CC, CN)) cm^{-1} that do not have strong counterparts in the ground-state spectrum, whereas the strongest ground-state δ(bpy-breathing)/δRebpy feature at 1033 cm^{-1} shifts to ~1008 cm^{-1} and decreases in intensity. The low-frequency region exhibits features due to deformation vibrations of the $bpy^{\bullet-}$ ligand and the $Re^{II}(bpy^{\bullet-})$ chelate ring (522-525, 632, ~661, 710 cm^{-1}), an Re-CO stretch at 375, 402-409, 436-443 cm^{-1}, and ReCO deformations (436-443, ~471, 539–593 cm^{-1}). The principal mode involving the Re-Cl stretch was observed at 266–277 cm^{-1}. ν(ReCl) also contributes to the features at 245–253 and ~200 cm^{-1}, coupled with out-of-plane $bpy^{\bullet-}$ and $Re^{II}(bpy^{\bullet-})$ deformations.

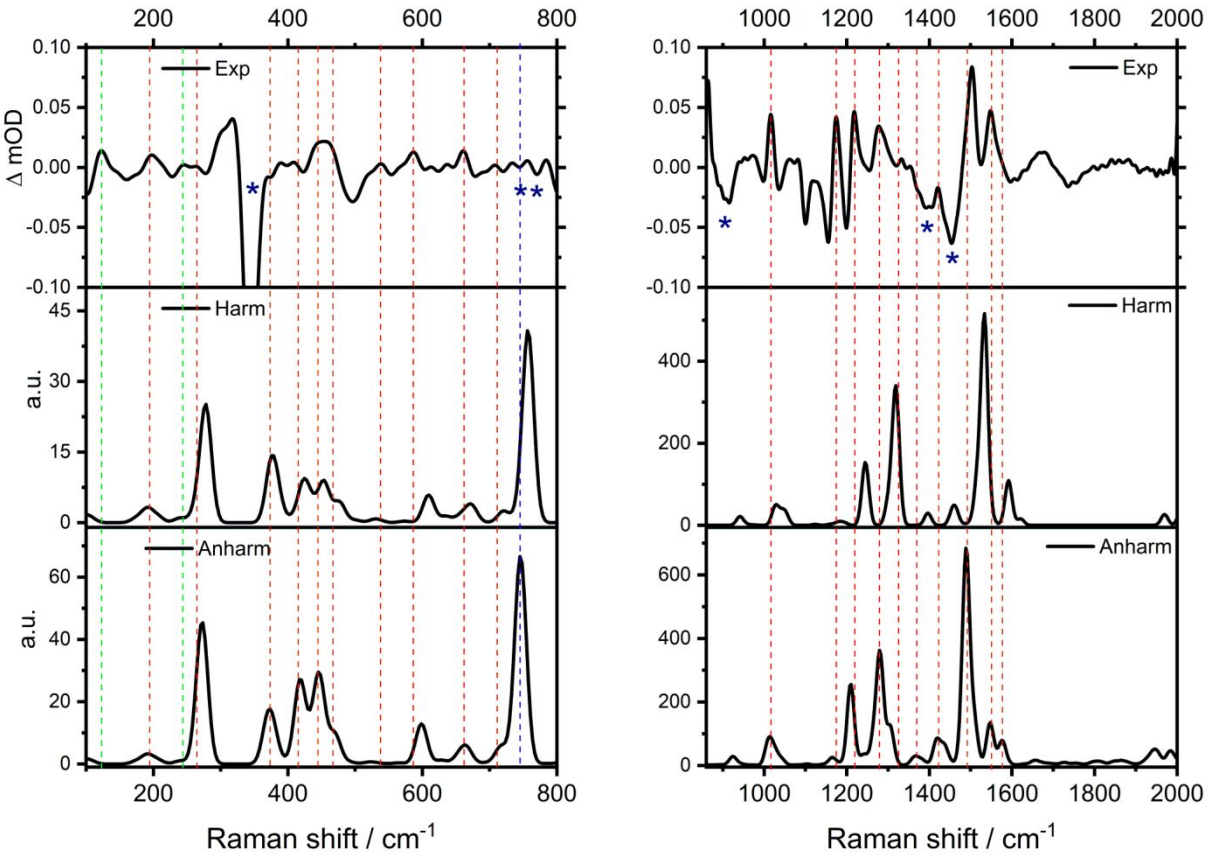

Figure 2. FSRS of the lowest electronic excited state of $ReCl(CO)_3(bpy)$ in CD_3CN measured 60 ps after 400 nm excitation (top), together with harmonically (middle) and anharmonically (bottom) calculated Raman spectra. Red lines connect experimental and corresponding anharmonically calculated Raman features. Green lines show experimental Raman bands without obvious calculated counterparts. Blue line: Calculated band without an experimental counterpart presumably due to overlapping solvent features. * denotes residual solvent features and background artifacts. No experimental features detected between 2000 and 4000 cm^{-1}. Spectra measured in CH_3CN are shown in Figure S3. (a.u. = arbitrary units)

Table 2. Experimental[a] and calculated Raman spectra of the lowest electronic excited state $ReCl(CO)_3(bpy)$.

#[b]	Principal vibrations [c]	Experimental	Harmonic	Anharmonic	Relative int. [c]
70	$\nu(CO)_{sym}$	2053	2086	2052	100
69	$\nu(CO)_{ax} + \nu(CO)_{sym,eq}$	1985	2012	1981	4.7
68	$\nu(CO)_{asym,eq}$	1940	1969	1945	4.3
	63 + 18	1868 (1884)	-	1865	0.8
67	ν(CC, CN)	1579 (1577)[d]	1621	1576*	3.6

66	ν(CC, CN)	1548 (1550)	1592	1546*	18.3
64	ν(CC inter-ring) + ν(CC)	1500 (1502)	1534	1490*	72.4
63	ν(CC, CN, CC inter-ring)	1477 (1482) shoulder	1516	1484*	2.1
60	δ(CH) + ν(CN, CC inter-ring)	1422 (1421)	1456	1417	11.9
59	ν(CC inter-ring) + δ(CH)	(1370)	1396	1363	3.3
57	ν(CN, CC)	1279 (1277)	1318	1280*	52
55	δ(CH)	1217 (1218)	1245	1209*	39
53	δ(CH)	1175 (1173)	1179	1164	3.3
	27 overtone	1057	-	1042	1.9
48	ν(CC) + ν(CN)	1008 (1016)	1038	1021*	3.6
47	δ(bpy-breath) + δ(Rebpy)		1027	1010*	9.1
	31 + 18	980 (972)	-	977	0.1
	25 overtone	-	-	940	0.3
42	$\delta(\text{bpy-breath})_{\text{antisym}}$ + δ(Rebpy)			923	4
40	$\delta(\text{CH})_{\text{antisym, out-plane}}$	843 815	836	824	0.3 0.3
38	$\delta(\text{bpy-breath})_{\text{sym}}$	767	757	746	9.3
36	$\delta(\text{bpy})_{\text{out-plane}}$	711 (708)	720	716	0.6
35	$\delta(\text{bpy})_{\text{out-plane}}$	~650, 684 (661)	681	671	0.1
34	δ(bpy) + δ(Rebpy)		672	665	0.7
33	δ(bpy) + δ(Rebpy)		657	654	0.6
32	δ(bpy) + δ(Rebpy)	632	635	628	0.2
31	δ(Re-C-O)	597 (587)	609	599*	2
30[e]	δ(Re-C-O)	559 (539)	573?	564?	0.1
28	$\delta(\text{bpy})_{\text{out-plane}}$	525 (522)	529	520	0.1
27	δ(Re-C-O) + $\delta(\text{bpy})_{\text{out-plane}}$	-	500	492	0.1
26	δ(Re-C-O) + $\delta(\text{bpy})_{\text{out-plane}}$	470 (~472)	477	471*	1.2
25	δ(Re-C-O) + δ(bpy)	-	466	463	0.4
24	$\nu(\text{Re-CO})_{\text{eq}}$ + $\delta(\text{Re-C-O})_{\text{ax}}$ + δ(Rebpy)	436 (443)	453	447*	4.1
23	$\delta(\text{bpy})_{\text{out-plane}}$ + δ(Re-C-O)		437	436*	0.7
21	$\nu(\text{Re-CO})_{\text{ax}}$ + $\delta(\text{bpy})_{\text{out-plane}}$	402 (409)	423	418	3.5
18	$\nu(\text{Re-CO})_{\text{eq,antisym}}$ + δ(Rebpy)	(375)	384	379	1
17	$\delta(\text{bpy})_{\text{out-plane}}$		375	370*	2.1
16	ν(ReCl) + δ(Rebpy)	277 (266)	278	273*	6.9
15	δ(Rebpy) + ν(ReCl)	253 (245)	263	263*	0.4
14	$\delta(\text{bpy})_{\text{out-plane}}$	236	239	239	0.2
13	$\delta(\text{bpy})_{\text{out-plane}}$	213	206	206	0.2
12	$\delta(\text{bpy})_{\text{out-plane}}$ + δ(Re-Cl)	200 (198)	191	191*	0.4
11	$\delta(\text{bpy})_{\text{out-plane}}$ + δ(Rebpy)		175	175	0.1
10	Deformation	128 (122)	106	106	0.1

[a] Data from CH_3CN or (CD_3CN) solutions. No features detected between 2000 and 4000 cm^{-1}. [b] Normal mode number in the order of increasing frequency. [c] Based on anharmonic calculation.

Deformations of the Rebpy moiety (δ(Rebpy)) involve ReN stretches. [d] Determined by Gaussian decomposition, see the text. [e] Tentative assignment (calculated with a very small intensity). * Vibration shown in Chart S2.

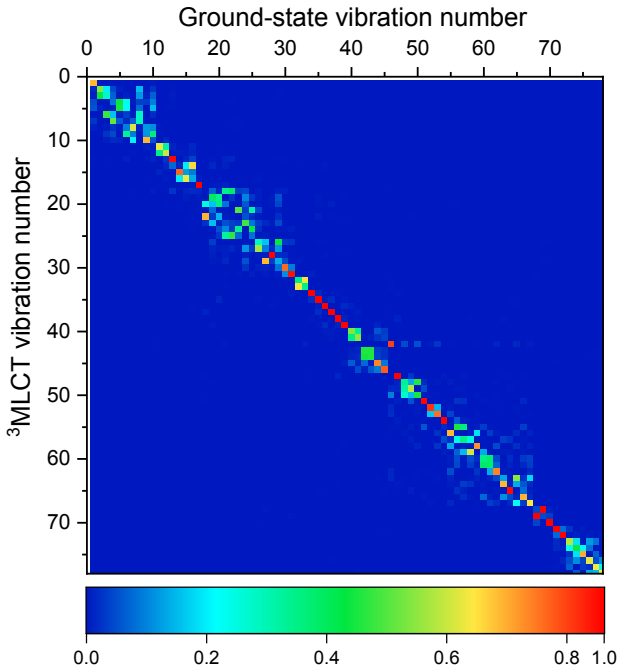

Figure 3. Duschinsky matrix of anharmonically calculated vibrations of $ReCl(CO)_3(bpy)$ in the ground- and lowest ^{3}MLCT states. The matrix shows excited-state vibrations as a linear combination of ground-state vibrations (horizontally) and vice-versa (vertically). The corresponding shift-vector diagram is shown in Figure S5.

Time-resolved excited-state Raman spectra (Figures 4, S6) show dramatic changes in the 1450–1600 cm^{-1} region where a group of features due to high-frequency $bpy^{\bullet-}$ CC and CN stretching vibrations 63–67 emerges between 150 and 200 fs and then grows over the next few tens of picoseconds (Figures 5A, B). The integrated area of the corresponding bands grows with a biexponential kinetics (380 fs, 65%; 21 ps, 35%; Figures 5C and S7). Bandwidths show a small initial rise followed by narrowing with a maximum at ~3 ps (for the 1551 cm^{-1} band, Figure 5D). The peak maximum of the strongest band shifts from 1496 cm^{-1} at 200 fs to 1502 cm^{-1} at 30 ps and later. The ~1546 cm^{-1} feature undergoes a small upshift and band-shape changes. More

pronounced restructuring of the 1450–1600 cm^{-1} spectral pattern takes place at the earliest investigated times, from 40 to 200 fs (Figure 5B). The initial spectrum recorded at 40 fs shows spectral features at ca. 1486, 1514, 1532, and 1552 cm^{-1} that all gradually shift to higher wavenumbers. The 1514 cm^{-1} band concomitantly decreases in intensity and eventually (200–300 fs) disappears, whereas the latter two merge into the 1546 cm^{-1} feature showing a ~1573 cm^{-1} shoulder. Mid-range spectral features are largely developed already at 150 fs and show only limited dynamics, usually small picosecond upshifts and growth, commensurate with the ~21 ps growth component identified in the 1450–1600 cm^{-1} range. This is the case, for example, of the bands at 1212 and 1273 cm^{-1} that shift to ~1217 and ~1278 cm^{-1}, respectively, while that at 1171 cm^{-1} moves less, to 1174 cm^{-1}. More interesting dynamics occurs in the low-frequency range (Figure 6), where the features at 583 and 665 cm^{-1} (in CD_3CN) and 560–585 cm^{-1} (CH_3CN) decrease in intensity during the first 300 fs whereas the lowest band increases and shifts from ~112 (at 150 fs) to 124 cm^{-1} during the first 2 ps. Early band restructuring around 200 and ~580 cm^{-1} will be discussed below, in the context of intersystem crossing.

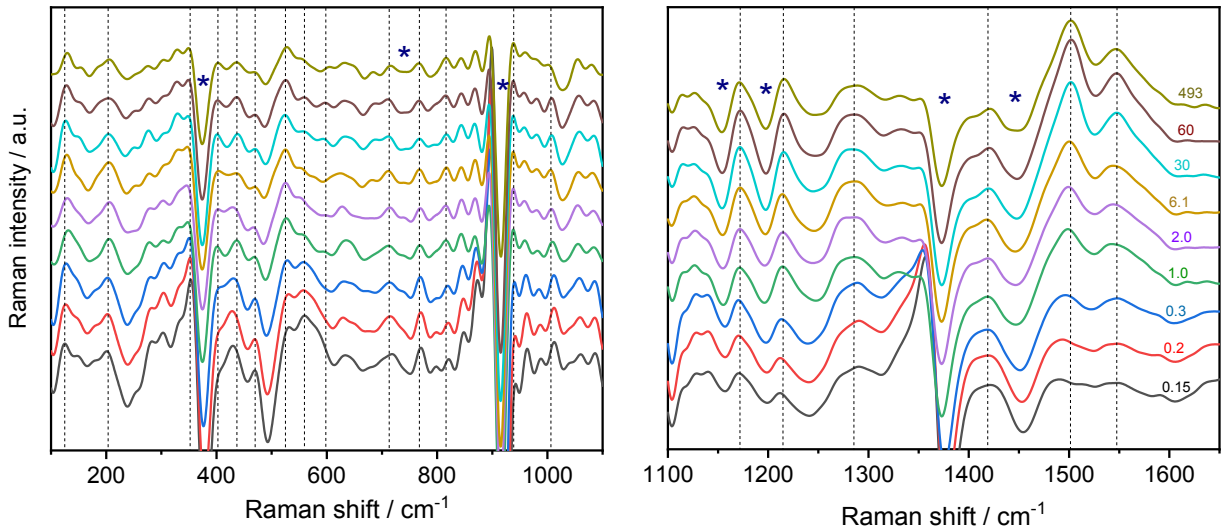

Figure 4. Time evolution of FSRS of $ReCl(CO)_3(bpy)$ in CH_3CN measured (from bottom to the top) at 0.15, 0.2, 0.3, 1.0, 2.0, 6.1, 30, 60, and 493 ps. The spectra are offset by a constant amount for better visibility. The dotted lines show band positions in the 60 ps spectrum. * Solvent or background features. Spectra in CD_3CN are shown in Figure S6.

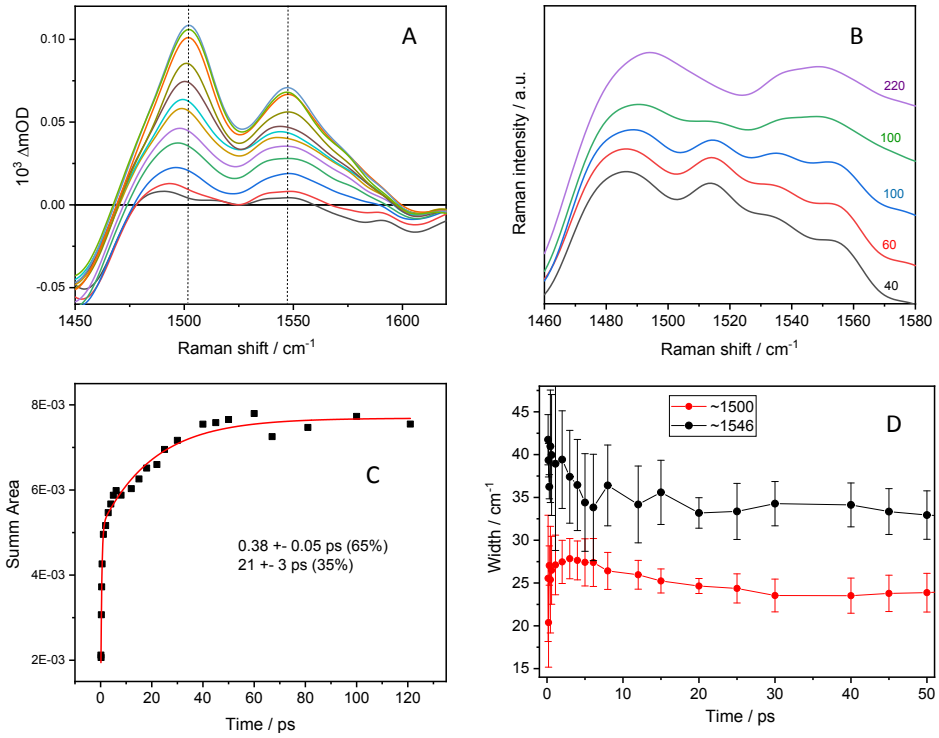

Figure 5. Dynamics of Raman bands in the 1450–1600 cm^{-1} range measured in CH_3CN. A: Time-resolved spectra adjusted to a common zero-signal level. Time delays from bottom up: 0.15, 0.20, 0.30, 0.45, 0.61, 1.1, 2.0, 6.1, 14.9, 30, 60, 122 ps. The dotted lines show band positions in the 60 ps spectrum. B: Detail of the spectral evolution from 40 to 220 fs; spectra are offset by a constant amount. C: Time-dependence of the sum of band areas in the 1450–1600 cm^{-1} range. (Time-dependence of the ~1500 cm^{-1} band area alone is shown in Figure S7.) D: Time-dependence of the widths (fwhm) of ~1500 and 1546 cm^{-1} Raman features. (Band areas and widths were obtained by Gaussian decomposition.)

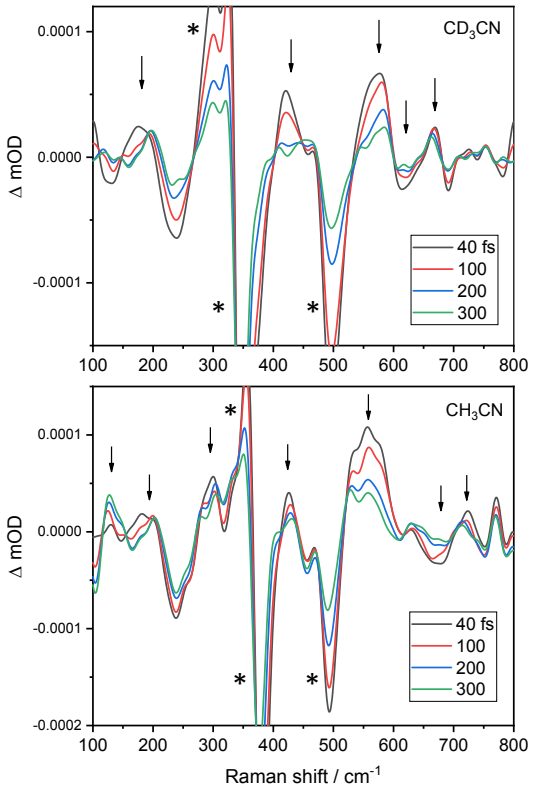

Figure 6. Early FSRS evolution of $ReCl(CO)_3(bpy)$ in CD_3CN (top) and CH_3CN (bottom). Spectra are adjusted to a common zero-signal level. * denote incompletely subtracted / shifted solvent bands. The spectra were not corrected for the difference in Raman pump absorption between actinic-pumped and non-actinic pumped FSRS that causes intensity variations of the negative solvent peaks whereas positive excited-state feature are affected much less since the ground-state $ReCl(CO)_3(bpy)$ is several orders of magnitude weaker.

■ DISCUSSION

Ground- and excited-state Raman spectra (FSRS) measured over a full relevant spectral range together with a computational anharmonic vibrational analysis characterize bonding and structural changes upon excitation, while the temporal evolution of the spectra provides information on excited-state relaxation processes that take place on femtosecond to early picosecond timescale.

Calculations show that most vibrational modes are delocalized over several bonds and molecular fragments (Charts S1, S2). Nevertheless, it is possible to identify groups of vibrations of similar principal contributions (Tables 1, 2). Going up from the lowest energies, these are bpy and ReCO deformations coupled with Re-Cl stretches, deformations coupled with Re-CO stretches, a group of bpy and Re(bpy) deformations (the latter involving Re-N stretching motions), C-H deformations, inter-ring CC stretch coupled with CC and/or CN stretches of the bpy ligand, and CC/CN stretching motions of the aromatic rings. CO vibrations around 2000 cm^{-1} give rise only to very weak features in the ground-state spectrum. They are entirely absent in the excited-state spectra, presumably due to the lack of resonance enhancement. FSRS peak wavenumbers in the high-frequency range agree with those observed in TR^3 spectra of $ReCl(CO)_3(bpy)$.[26] The relative band intensities are, however, different because the TR^3 spectra were measured using 400 nm Raman pump whose proximity to the most intense excited-state electronic absorption band at 373 nm causes much stronger resonance enhancement than 800 nm pumping, where the transient absorption is much weaker (Figure S1C, oscillator strengths in the legend).[26,51,52] Interestingly, excited-state FSRS frequencies and intensity patterns of $ReCl(CO)_3(bpy)$ at 60 ps are very similar to those measured at 100 fs and later for $[Ru(bpy)_3]^{2+}$ in the 1100–1700 cm^{-1} range using a virtually identical pump wavelength (801 nm).[55] The close similarity of excited-state bpy-based Raman features of the complexes with one (Re) and three bpy ligands (Ru) shows that the charge localization at a single bpy in ^{3}MLCT-excited $[Ru(bpy)_3]^{2+}$ occurs in much less than 100 fs.

Shifts of Raman features from the ground-state spectrum to the 60 ps spectrum of the relaxed lowest excited state are in agreement with bonding changes expected for the

$ReCl(CO)_3 \rightarrow$bpy CT character of the lowest excited state:[15,56,57,58,59,60] The bpy-localized LUMO that becomes singly populated in the excited state is π-bonding with respect to the inter-ring C-C bond and π-antibonding toward the ring CN and CC bonds (Figure S8).[57] Accordingly, the predominantly inter-ring ν(CC) ground-state mode 58 shifts ~52 cm^{-1} higher upon excitation (contributing 61% to the excited-state mode 59, based on the Duschinsky matrix). Modes 60 and 63, which also have a ν(CC-inter-ring) contribution, transform to 60+61 and 64, respectively, in the excited state. Each occur ca. 10 cm^{-1} higher than in the ground state. Bands due to predominantly intra-ring CC and CN stretching vibrations shift downwards upon excitation because of a LUMO π^* character. This is the case of the ground-state mode 66 that amounts to 69% of the excited state mode 66, which lies ca. 55 cm^{-1} lower. Frequencies of the modes with significant ν(Re-CO) contributions, namely 23 and 25 (that remix to form excited-state modes 21 and 24) decrease on average by ~68 cm^{-1}. The ν(Re-C) downshift is complementary to the upshift of ν(C≡O) vibrations that has been amply demonstrated by TRIR spectroscopy.[15,22,23,26] Both these effects are caused by decreased Re$\rightarrow$CO π back-bonding in the ^{3}MLCT excited state due to depopulation of the Re-CO π-bonding / C≡O π-antibonding HOMO (Figure S8), weakening and strengthening Re-CO and C≡O bonds, respectively. Downshifting ν(Re-CO) Raman features upon excitation provides additional evidence for the principal $Re(CO)_3 \rightarrow$bpy contribution to the lowest excited state. It also agrees with the calculated lengthening of axial and equatorial Re-CO bonds when going to the lowest excited state by 0.048 and 0.041 Å, respectively.[61] On the other hand, modes involving the Re-Cl stretching motion shift up by ca. 10 cm^{-1}, which is attributable to the depopulation of the Re-Cl π-antibonding Re(dπ)-Cl(pπ) HOMO (Figure S8). In particular, the ν(ReCl)-containing ground-

state modes 14-16 participate in excited-state ν(ReCl) modes 15 and 16 that lie, on average lie 10 cm^{-1} higher. The upshift of ν(ReCl) vibrations upon excitation is the third experimental piece of evidence for the Cl→bpy CT contribution to the excited-state wave function, after the TRIR spectra of $Re(NCS)(CO)_3(bpy)$ and time-resolved X-ray absorption of $ReBr(CO)_3(bpy)$.[57,58,59]

The temporal evolution of the Raman spectra (Figures 4-6, S6) provides insight into the mechanism of the lowest excited-state population and its relaxation. Interestingly, individual Raman bands show different dynamics. High-frequency bands due to bpy-localized CC, CN, and inter-ring C-C stretching vibrations in the 1450–1600 cm^{-1} range are initially nearly absent (Figure 5). At 40-100 fs, four very weak bands are observed that blue-shift and merge into two broad features between 200 and 300 fs (Figure 5B). Subsequently, they grow with biexponential kinetics (0.38 and 21 ps), eventually becoming the strongest features in the 60-ps spectrum of the relaxed ^{3}MLCT state. This behavior cannot be attributed to increasing resonance enhancement as the transient absorption at and around the 800 nm Raman pump is weak and partly decays during the first 2.5 ps (Figure S1). Femtosecond band restructuring was also observed for some of the low-frequency Raman bands, namely in the region of ν(ReCl)/deformation vibrations around 190-200 cm^{-1}, and δ(Re-C-O) bending vibrations around 420–440 and 520–600 cm^{-1} (Figure 6). This mode-specific dynamics suggests that the electronic wave function (i.e., the excited-state character) changes in the course of relaxation. Initial time evolution in the 1450-1600 cm^{-1} spectral range agrees with the ultrafast fluorescence decay kinetics[52,61] whose 85 and 340 fs lifetimes were attributed to the intersystem crossing (ISC) from the optically populated ^{1}MLCT to an intermediate ππ*-bpy intraligand (^{3}IL) and to the lowest ^{3}MLCT excited states, combined with a ^{3}IL→^{3}MLCT conversion. This three-state (^{1}MLCT,

^{3}MLCT, ^{3}IL) model is a simplification since intersystem crossing actually proceeds through a manifold of intermediate states that arise from spin-orbit splitting of a number of intermediate ^{3}MLCT/^{3}IL states.[50,62,63,64,65,66,67] Quantum mechanical simulations of ultrafast excited-state dynamics of Re(halide)$(CO)_3$(bpy) complexes indicate that the initial ISC steps from the optically populated ^{1}MLCT occur in less than 20 fs. A more detailed ISC mechanistic picture was obtained by full-dimensional excited-state dynamics simulations of an analogous [Re(imidazole)$(CO)_3$(1,10-phenanthroline)]$^+$ complex, suggesting a two-phase ISC to the lowest triplet state.[63] In particular, a dynamic equilibrium between triplet and singlet MLCT states is established in less than 10 fs ("prompt ISC"). Then, convoluted intramolecular vibrational energy redistribution (IVR) and internal conversion shifts this equilibrium toward the lowest ^{3}MLCT state with a hundreds-of-femtoseconds time constant ("retarded ISC"). The latter process involves a gradually changing excited-state wave function whereby the IL ($\pi\pi^*$-bpy) contribution decreases and the MLCT character increases.[63] Our FSRS dynamics lends support to this model: The "instantaneous" change of the excited-state wave function is responsible for the presence of most of the excited-state Raman features in a few tens of femtoseconds, whereas the 40–200 fs restructuring of the ν(CC,CN) / $\nu(C\text{-}C)_{inter\text{-}ring}$ group of bands and its subsequent ~400 fs growth/upshift are attributable to the "retarded" ISC component. The ν(CC,CN)/$\nu(C\text{-}C)_{inter\text{-}ring}$ Raman features in the 1450–1600 cm^{-1} range are characteristic of the bpy$^{\bullet-}$ ligand and therefore develop and grow in intensity as the excited-state wave function acquires more $ReCl(CO)_3 \rightarrow$bpy CT character. This process continues well into the picosecond time domain (21 ps rise) as the solvational and vibrational relaxation drives the intramolecular charge separation further. These Raman dynamics are consistent with the picosecond growth of

a $bpy^{\bullet-}$-specific ~380 nm band in the TA spectra[26,52] and with the behavior of ν(C≡O) features in TRIR spectra that shift to higher wavenumbers with 1.5 and 12.6 ps time constants and also indicate the presence of another excited state with more ^{3}IL character.[26,52,68] FSRS dynamics in the low-frequency range mostly concerns features due to vibrational modes that involve ν(Re-Cl) and δ(Re-C-O) motions that were found[69] to be strongly coupled to the ISC process. In fact, the 40–100 fs spectra show shallow shifting minima at 130–160 and ~690 cm^{-1} that develop into weak positive features in few hundreds of femtoseconds. These minima might arise from inverse Raman scattering[34] due to vibrations that were activated in the course of ISC, as has been predicted theoretically.[69] Other spectral features exhibit very limited dynamics, usually small picosecond upshifts and growths, generally commensurate with the ~21 ps growth component identified in the 1450–1600 cm^{-1} range and mostly attributed to solvational relaxation. Interestingly, the FSRS excited-state dynamics of $ReCl(CO)_3(bpy)$ is more complex than that of $[Ru(bpy)_3]^{2+}$ that shows[55] a monotonous ~110 fs growth of $bpy^{\bullet-}$ features. The difference is attributable to the time-dependent mixing of IL($\pi\pi$*-bpy) and CT characters in the lowest excited state of the rhenium complex, in contrast to a virtually pure MLCT character in the ruthenium case. Furthemore, the low-symmetry and the presence of ligands with different polarities and solvation properties make $ReCl(CO)_3(bpy)$ much more susceptible to solvation dynamics.

■ CONCLUSIONS

Time-resolved FSRS of the lowest excited state of a prototypical organometallic photosensitizer/photocatalyst $ReCl(CO)_3(bpy)$ measured from ~40 to 2000 cm^{-1} with ca. 40 fs time resolution have demonstrated that:

- Good quality FSRS can be measured in the low-wavenumber region (40–800 cm^{-1}) when the Raman probe continuum is generated with laser pulses of a wavelength (1400 nm) substantially longer than that of the Raman pump (800 nm). "Watermarking",[29] whereby a set of spectra measured at 96 slightly different Raman pump wavelengths is used to reconstruct the final spectrum, improves the experiment sensitivity, background rejection, and the S/N ratio.

- Anharmonic calculations based on DFT and second-order vibrational perturbation theory provide vibrational frequencies that match the experimental Raman shift wavenumbers with accuracy sufficient to interpret experimental spectra, identify weak features, and with the possibility to predict spectra of electronically excited species and photochemical intermediates.

- Shifts of Raman features upon excitation (ν(ReCl) and ν(CC-inter-ring) upwards, ν(CC, CN) and ν(Re-C) downwards) agree with the predominant $ReCl(CO)_3 \rightarrow$bpy CT character of the lowest excited state, demonstrating the diagnostic value of low-frequency Raman modes in excited-state characterization and the need for reliable assignment provided by anharmonic calculations.

- Temporal evolution of FSRS features is mode-specific and provides information on the dynamics and mechanism of the population of the lowest excited state and its relaxation, namely the development of the charge separation in the relaxed MLCT state.

FSRS experiments coupled with perturbational anharmonic calculations emerge as a promising tool to investigate the rich excited-state chemistry of Re carbonyl-diimine photosensitizers and photocatalysts.

■ AUTHOR INFORMATION

Corresponding Authors
*E-mail: Miroslav.Kloz@eli-beams.eu
*E-mail: a.vlcek@qmul.ac.uk

ORCID
Alessandra Picchiotti: 0000-0003-0167-1431
MateuszRebarz: 0000-0002-5823-2432
Nils Lenngren: 0000-0001-7563-9843
Yingliang Liu: 0000-0002-4089-688X
Stanislav Záliš: 0000-0003-4345-3205
Miroslav Kloz: 0000-0003-4609-8018
Antonín Vlček: 0000-0002-6413-8311

Notes
The authors declare no competing financial interest

■ ACKNOWLEDGMENTS

This work was supported by the Czech Science Foundation (GAČR) grant 17-011375 and EPSRC (UK) grant EP/R029687/1, as well as the Projects ELIBIO (CZ.02.1.01/0.0/0.0/15_003/0000447) and ADONIS (CZ.02.1.01/0.0/0.0/16_019/0000789) from the European Regional Development Fund.

■ ASSOCIATED CONTENT

Supporting Information Available
Transient absorption spectra, ground- and excited-state FSRS in CH_3CN, detailed Duschinsky matrices, time-resolved FSRS in CD_3CN, visualization of selected ground- and excited-state vibrations.
This information is available free of charge via the Internet at https://pubs.acs.org/.

References

1. Vlček, A.; Kvapilová, H.; Towrie, M.; Záliš, S., Electron-Transfer Acceleration Investigated by Time Resolved Infrared Spectroscopy. *Acc. Chem. Res.* **2015,** *48*, 868-876.

2. Dereka, B.; Koch, M.; Vauthey, E., Looking at Photoinduced Charge Transfer Processes in the IR: Answers to Several Long-Standing Questions. *Acc. Chem. Res.* **2017,** *50*, 426−434.
3. Kukura, P.; Yoon, S.; Mathies, R. A., Femtosecond Stimulated Raman Spectroscopy. *Anal. Chem.* **2006,** *78*, 5952-5959.
4. Frontiera, R. R.; Mathies, R. A., Femtosecond Stimulated Raman Spectroscopy. *Laser Photonics Rev.* **2011,** *5*.
5. Brown, K. E.; Veldkamp, B. S.; Co, D. T.; Wasielewski, M. R., Vibrational Dynamics of a Perylene−Perylenediimide Donor−Acceptor Dyad Probed with Femtosecond Stimulated Raman Spectroscopy. *J. Phys. Chem. Lett.* **2012** *3*,2362−2366.
6. Dietze, D. R.; Mathies, R. A., Femtosecond Stimulated Raman Spectroscopy. *ChemPhysChem* **2016,** *17*, 1224-1251.
7. Hoffman, D. P.; Mathies, R. A., Femtosecond Stimulated Raman Exposes the Role of Vibrational Coherence in Condensed-Phase Photoreactivity. *Acc. Chem. Res.* **2016,** *49*, 616−625.
8. Ghosh, A.; Ostrander, J. S.; Zanni, M. T., Watching Proteins Wiggle: Mapping Structures with Two-Dimensional Infrared Spectroscopy. *Chem. Rev.* **2017,** *117*, 10726−10759.
9. Lima, M.; Candelaresi, M.; Foggia, P., 2D-IR Spectroscopy: An Additional Dimension to Investigate Ultrafast Structural Dynamics. *J. Raman Spectrosc.* **2013,** *44*, 1470–1477.
10. Latouche, C.; Palazzetti, F.; Skouteris, D.; Barone, V., High-Accuracy Vibrational Computations for Transition-Metal Complexes Including Anharmonic Corrections: Ferrocene, Ruthenocene, and Osmocene as Test Cases. *J. Chem. Theory Comput.* **2014,** *10*, 4565−4573.
11. Barone, V.; Biczysko, M.; Bloino, J., Fully Anharmonic IR and Raman Spectra of Medium-Size Molecular Systems: Accuracy and Interpretation. *Phys. Chem. Chem. Phys.* **2014,** *16*, 1759-1787.
12. Meinnel, J.; Latouche, C.; Ghanemi, S.; Boucekkine, A.; Barone, V.; Moréac, A.; Boudjada, A., Anharmonic Computations Meet Experiments (IR, Raman, Neutron Diffraction) for Explaining the Behavior of 1,3,5-Tribromo-2,4,6-trimethylbenzene. *J. Phys. Chem. A* **2016,** *120*, 1127−1132.
13. Bloino, J.; Biczysko, M., IR and Raman Spectroscopies beyond the Harmonic Approximation: The Second-Order Vibrational Perturbation Theory Formulation. *Reference Module in Chemistry, Molecular Sciences and Chemical Engineering, Elsevier:* **2015**.
14. Kvapilová, H.; Vlček, A., Jr.; Barone, V.; Biczysko, M.; Záliš, S., Anharmonicity Effects in IR Spectra of [Re(X)(CO)$_3$(α-diimine)] (α-diimine = 2,2′-bipyridine or pyridylimidazo[1,5‑a]pyridine; X = Cl or NCS) Complexes in Ground and Excited Electronic States. *J. Phys. Chem. A* **2015,** *119*, 10137−10146.
15. Vlček, A., Jr., Ultrafast Excited-State Processes in Re(I) Carbonyl-Diimine Complexes: From Excitation to Photochemistry. *Top. Organomet. Chem.* **2010,** *29*, 73-114.
16. Kumar, A.; Sun, S.-S.; Lees, A. J., Photophysics and Photochemistry of Organometallic Rhenium Diimine Complexes. *Top. Organomet. Chem.* **2010,** *29*, 1-35.
17. Lee, L. C.-C.; Leung, K.-K.; Lo, K. K.-W., Recent Development of Luminescent Rhenium(I) Tricarbonyl Polypyridine Complexes as Cellular Imaging Reagents, Anticancer Drugs, and Antibacterial Agents. *Dalton Trans.* **2017,** *46*, 16357–16380.
18. Hawecker, J.; Lehn, J.-M.; Ziessel, R., Efficient Photochemical Reduction of CO_2 to CO by Visible Light Irradiation of Systems Containing Re(X)(CO)$_3$(bpy) or Ru(bpy)$_3^{2+}$ -Co^{2+} Combination as Homogeneous Calysts. *J. Chem. Soc., Chem. Commun.* **1983**, 536-538.
19. Hawecker, J.; Lehn, J.-M.; Ziessel, R., Electrocatalytic Reduction of Carbon Dioxide Mediated by Re(bipy)(CO)$_3$Cl (bipy = 2,2'-bipyridine). *J. Chem. Soc., Chem. Commun.* **1984**, 328-330.
20. Hawecker, J.; Lehn, J.-M.; Ziessel, R., Photochemical and Electrochemical Reduction of CO_2 to CO Mediated by Re(Cl)(CO)$_3$(bpy) and Related Complexes as Homogeneous Catalysts. *Helv. Chim. Acta* **1986,** *69*, 1990-2009.

21. Takeda, H.; Ishitani, O., Development of Efficient Photocatalytic Systems for CO_2 Reduction Using Mononuclear and Multinuclear Metal Complexes Based on Mechanistic Studies. *Coord. Chem. Rev.* **2010,** *254*, 346–354.
22. George, M. W.; Johnson, F. P. A.; Westwell, J. R.; Hodges, P. M.; Turner, J. J., Excited -state Properties and Reactivity of [Re(Cl)$(CO)_3$(bpy)] Studied by Time-Resolved Infrared Spectroscopy. *J. Chem. Soc., Dalton Trans.* **1993**, 2977-2979.
23. Dattelbaum, D. M.; Omberg, K. M.; Hay, P. J.; Gebhart, N. L.; Martin, R. L.; Schoonover, J. R.; Meyer, T. J., Defining Electronic Excited States Using Time-Resolved Infrared Spectroscopy and Density Functional Theory Calculations. *J. Phys. Chem. A* **2004,** *108*, 3527-3536.
24. Blanco-Rodríguez, A. M.; Towrie, M.; Sýkora, J.; Záliš, S.; Vlček, A., Jr., Photoinduced Intramolecular Tryptophan Oxidation and Excited-State Behavior of $[Re^{I}$(L-AA)$(CO)_3$(diimine)$]^+$ (L = pyridine or imidazole, AA = tryptophan, tyrosine, phenylalanine) *Inorg. Chem.* **2011,** *50*, 6122–6134.
25. Blanco-Rodríguez, A. M.; Ronayne, K. L.; Záliš, S.; Sýkora, J.; Hof, M.; Vlček, A., Jr., Solvation-Driven Excited-State Dynamics of [Re(4-Et-pyridine)$(CO)_3$(2,2'-bipyridine)$]^+$ in Imidazolium Ionic Liquids. A Time-Resolved Infrared and Phosphorescence Study. *J. Phys. Chem. A* **2008,** *112*, 3506-3514.
26. Liard, D. J.; Busby, M.; Matousek, P.; Towrie, M.; Vlček, A., Jr., Picosecond Relaxation of ^{3}MLCT Excited States of [Re(Etpy)$(CO)_3$(dmb)$]^+$ and [Re(Cl)$(CO)_3$(bpy)] as Revealed by Time-Resolved Resonance Raman, IR and UV-Vis Absorption Spectroscopy. *J. Phys. Chem. A* **2004,** *108*, 2363-2369.
27. Smothers, W. K.; Wrighton, M. S., Raman Spectroscopy of the Ground and MLCT Excited Re(Cl)$(CO)_3$(bpy) and Ru$(bpy)_3$. *J. Am. Chem. Soc.* **1983,** *105*, 1067-1069.
28. Worl, L. A.; Duesing, R.; Chen, P.; Della Ciana, L.; Meyer, T. J., Photophysical Properties of Re(Cl)$(CO)_3(X_2$-bpy). *J. Chem. Soc. Dalton Trans.* **1991**, 849-858.
29. Kloz, M.; Weissenborn, J.; Polívka, T.; Frank, H. A.; Kennis, J. T. M., Spectral Watermarking in Femtosecond Stimulated Raman Spectroscopy: Resolving the Nature of the Carotenoid S* State. *Phys. Chem. Chem. Phys.* **2016,** *18*, 14619-14628.
30. McCamant, D. W.; Kukura, P.; Yoon, S.; Mathies, R. A., Femtosecond Broadband Stimulated Raman Spectroscopy: Apparatus and Methods. *Rev. Sci. Instrum.* **2004,** *75*, 4971–4980.
31. Laimgruber, S.; Schachenmayr, H.; Schmidt, B.; Zinth, W.; Gilch, P., A Femtosecond Stimulated Raman Spectrograph for the Near Ultraviolet. *Appl. Phys. B-Lasers Opt.* **2006,** *85*, 557–564
32. Brunsgaard-Hansen, S.; Berg, R. W.; Stenby, E. H., Upgrade of a Raman Spectrometer. *Appl. Spectrosc. Rev.* **2004,** *39*, 385-397.
33. Oscar, B. G.; Chen, C.; Liu, W.; Zhu, L.; Fang, C., Dynamic Raman Line Shapes on an Evolving Excited-State Landscape: Insights from Tunable Femtosecond Stimulated Raman Spectroscopy. *J. Phys. Chem. A* **2017,** *121*, 5428−5441.
34. Weigel, A.; Ernsting, N. P., Excited Stilbene: Intramolecular Vibrational Redistribution and Solvation Studied by Femtosecond Stimulated Raman Spectroscopy. *J. Phys. Chem. B* **2010,** *114*, 7879–7893.
35. Kloz, M.; van Grondelle, R.; Kennis, J. T. M., Wavelength-Modulated Femtosecond Stimulated Raman Spectroscopy - Approach Towards Automatic Data Processing. *Phys. Chem. Chem. Phys.* **2011,** *13*, 18123-18133.
36. Wende, T.; Liebel, M.; Schnedermann, C.; Pethick, R. J.; Kukura, P., Population-Controlled Impulsive Vibrational Spectroscopy: Background- and Baseline-Free Raman Spectroscopy of Excited Electronic States. *J. Phys. Chem. A* **2014,** *118*, 9976−9984.
37. Kuramochi, H.; Takeuchi, S.; Kamikubo, H.; Kataoka, M.; Tahara, T., Fifth-Order Time-Domain Raman Spectroscopy of Photoactive Yellow Protein for Visualizing Vibrational Coupling in its Excited State. *Sci. Adv.* **2019,** *5*, eaau4490.
38. Frisch, M. J.; Trucks, G. W.; Schlegel, H. B.; Scuseria, G. E.; Robb, M. A.; Cheeseman, J. R.; Scalmani, G.; Barone, V.; Petersson, G. A.; Nakatsuji, H.; et al. *Gaussian16, Revision A.03*, Gaussian, Inc.: Wallingford, CT, 2016.

39. Becke, A. D., Density-Functional Thermochemistry. III. The Role of Exact Exchange. *J. Chem. Phys.* **1993,** *98*, 5648-5652.
40. Lee, C.; Yang, W.; Parr, R. G., Development of the Colic-Salvetti Correlation-Energy Formula into a Functional of the Electron Density. *Phys. Rev. B* **1988,** *37*, 785-789.
41. Andrae, D.; Häussermann, U.; Dolg, M.; Stoll, H.; Preuss, H., Energy-Adjusted ab initio Pseudopotentials for the Second and Third Row Transition Elements. *Theor. Chim. Acta* **1990,** *77*, 123-141.
42. Martin, J. M. L.; Sundermann, A., Correlation Consistent Valence Basis Sets for Use with the Stuttgart–Dresden–Bonn Relativistic Effective Core Potentials: The Atoms Ga–Kr and In–Xe. *J. Chem. Phys.* **2001,** *114*, 3408-3420.
43. Krishnan, R.; Binkley, J. S.; Seeger, R.; Pople, J. A., Self-Consistent Molecular Orbital Methods. XX. A Basis Set for Correlated Wave Functions. *J. Chem. Phys.* **1980,** *72*, 650-654.
44. Cossi, M.; Rega, N.; Scalmani, G.; Barone, V., Energies, Structures, and Electronic Properties of Molecules in Solution with the C-PCM Solvation Model. *J. Comput. Chem.* **2003,** *24*, 669-681.
45. Barone, V.; Bloino, J.; Guido, C. A.; Lipparini, F., A Fully Automated Implementation of VPT2 Infrared Intensities. *Chem. Phys. Lett.* **2010,** *496*, 157-161.
46. Barone, V.; Biczysko, M.; Bloino, J.; Borkowska-Panek, M.; Carnimeo, I.; Panek, P., Toward Anharmonic Computations of Vibrational Spectra for Large Molecular Systems. *Int. J. Quantum Chem.* **2012,** *112*, 2185-2200.
47. Bloino, J.; Biczysko, M.; Barone, V., Anharmonic Effects on Vibrational Spectra Intensities: Infrared, Raman, Vibrational Circular Dichroism, and Raman Optical Activity. *J. Phys. Chem. A* **2015,** *119*, 11862-11874.
48. Piccardo, M.; Bloino, J.; Barone, V., Generalized Vibrational Perturbation Theory for Rotovibrational Energies of Linear, Symmetric and Asymmetric Tops: Theory, Approximations, and Automated Approaches to Deal with Medium-to-Large Molecular Systems. *Int. J. Quantum Chem.* **2015,** *115*, 948-982.
49. Licari, D.; Baiardi, A.; Biczysko, M.; Egidi, F.; Latouche, C.; Barone, V., Implementation of a Graphical User Interface for the Virtual Multifrequency Spectrometer: The VMS-Draw Tool. *J. Comput. Chem.* **2015,** *36*, 321-334.
50. Heydová, R.; Gindensperger, E.; Romano, R.; Sýkora, J.; Vlček, A., Jr.; Záliš, S.; Daniel, C., Spin-Orbit treatment of UV-vis Absorption Spectra and Photophysics of Rhenium(I) Carbonyl-Bipyridine Complexes: MS-CASPT2 and TD-DFT Analysis. *J. Phys. Chem. A* **2012,** *116*, 11319−11329.
51. Záliš, S.; Consani, C.; El Nahhas, A.; Cannizzo, A.; Chergui, M.; Hartl, F.; Vlček, A., Jr., Origin of Electronic Absorption Spectra of MLCT-Excited and One-Electron Reduced 2,2'-bipyridine and 1,10-phenanthroline Complexes. *Inorg. Chim. Acta* **2011,** *374*, 578–585.
52. El Nahhas, A.; Cannizzo, A.; van Mourik, F.; Blanco-Rodríguez, A. M.; Záliš, S.; Vlček, A., Jr.; Chergui, M., Ultrafast Excited-State Dynamics of $[Re(L)(CO)_3(bpy)]^n$ Complexes: Involvement of the Solvent *J. Phys. Chem. A* **2010,** *114*, 6361-6369.
53. Kiefer, L. M.; King, J. T.; Kubarych, K. J., Equilibrium Excited State Dynamics of a Photo-Activated Catalyst Measured with Ultrafast Transient 2DIR. *J. Phys. Chem. A* **2014,** *118*, 9853−9860.
54. Kiefer, L. M.; King, J. T.; Kubarych, K. J., Dynamics of Rhenium Photocatalysts Revealed through Ultrafast Multidimensional Spectroscopy. *Acc. Chem. Res.* **2015,** *48*, 1123−1130.
55. Yoon, S.; Kukura, P.; Stuart, C. M.; Mathies, R. A., Direct Observation of the Ultrafast Intersystem Crossing in Tris(2,2'-bipyridine)ruthenium(II) using Femtosecond Stimulated Raman Spectroscopy. *Mol. Phys.* **2006,** *104*, 1275-1282.
56. Stufkens, D. J.; Vlček, A., Jr., Ligand-Dependent Excited State Behaviour of Re(I) and Ru(II) Carbonyl-Diimine Complexes. *Coord. Chem. Rev.* **1998,** *177*, 127-179.

57. Blanco-Rodríguez, A. M.; Gabrielsson, A.; Motevalli, M.; Matousek, P.; Towrie, M.; Šebera, J.; Záliš, S.; Vlček, A., Jr., Ligand-to-Diimine / Metal-to-Diimine Charge-Transfer Excited States of [Re(NCS)(CO)$_3$(α-diimine)] (α-diimine = 2,2'-bipyridine, di-iPr-N,N-1,4-diazabutadiene). A Spectroscopic and Computational Study. *J. Phys. Chem. A* **2005,** *109*, 5016-5025.
58. El Nahhas, A.; van der Veen, R. M.; Penfold, T. J.; Pham, V.-T.; Lima, F. A.; Abela, R.; Blanco-Rodríguez, A. M.; Záliš, S.; Vlček, A., Jr.; Tavernelli, I.; Rothlisberger, U.; Milne, C. J.; Chergui, M., X-Ray Absorption Spectroscopy of Ground and Excited Rhenium-Carbonyl-Diimine Complexes: Evidence for a Two-Centre Electron Transfer. *J. Phys. Chem. A* **2013,** *117*, 361-369.
59. Záliš, S.; Milne, C. J.; El Nahhas, A.; Blanco-Rodriguez, A. M.; van der Veen, R. M.; Vlček, A., Jr., Re and Br X-ray Absorption Near Edge Structure Study of the Ground and Excited States of [ReBr(CO)$_3$(bpy)] Interpreted by DFT and TD-DFT Calculations. *Inorg. Chem.* **2013,** *52*, 5775−5785.
60. Mai, S.; Plasser, F.; Dorn, J.; Fumanal, M.; Daniel, C.; González, L., Quantitative Wave Function Analysis for Excited States of Transition Metal Complexes. *Coord. Chem. Rev.* **2018,** *361*, 74–97.
61. Cannizzo, A.; Blanco-Rodríguez, A. M.; Nahhas, A.; Šebera, J.; Záliš, S.; Vlček, A., Jr.; Chergui, M., Femtosecond Fluorescence and Intersystem Crossing in Rhenium(I) Carbonyl-Bipyridine Complexes *J. Am. Chem. Soc.* **2008,** *130*, 8967-8974.
62. Baková, R.; Chergui, M.; Daniel, C.; Vlček, A., Jr.; Záliš, S., Relativistic Effects in Spectroscopy and Photophysics of Heavy-Metal Complexes Illustrated by Spin-Orbit Calculations of [Re(imidazole)(CO)$_3$(phen)]$^+$. *Coord. Chem. Rev.* **2011,** *255*, 975-989.
63. Mai, S.; González, L., Unconventional Two-Step Spin Relaxation Dynamics of [Re(CO)$_3$(im)(phen)]$^+$ in Aqueous Solution. *Chem. Sci.* **2019,** *10*, 10405–10411.
64. Mai, S.; Gattuso, H.; Fumanal, M.; Muñoz-Losa, A.; Monari, A.; Daniel, C.; González, L.; Webb, S. E. D., Excited States of a Rhenium Carbonyl Diimine Complex: Solvation Models, Spin–Orbit Coupling, and Vibrational Sampling Effects. *Phys. Chem. Chem. Phys.* **2017,** *19*, 27240-27250.
65. Fumanal, M.; Gindensperger, E.; Daniel, C., Ultrafast Excited-State Decays in [Re(CO)$_3$(N,N)(L)]$^{n+}$: Nonadiabatic Quantum Dynamics. *J. Chem. Theory Comput.* **2017,** *13*, 1293−1306.
66. Gourlaouen, C.; Eng, J.; Otsuka, M.; Gindensperger, E.; Daniel, C., Quantum Chemical Interpretation of Ultrafast Luminescence Decay and Intersystem Crossings in Rhenium(I) Carbonyl Bipyridine Complexes. *J. Chem. Theory Comput.* **2015,** *11*, 99−110.
67. Eng, J.; Gourlaouen, C.; Gindensperger, E.; Daniel, C., Spin-Vibronic Quantum Dynamics for Ultrafast Excited-State Processes. *Acc. Chem. Res.* **2015,** *48*, 809−817.
68. El Nahhas, A.; Consani, C.; Blanco-Rodríguez, A. M.; Lancaster, K. M.; Braem, O.; Cannizzo, A.; Towrie, M.; Clark, I. P.; Záliš, S.; Chergui, M.; Vlček, A., Jr., Ultrafast Excited-State Dynamics of Rhenium(I) Photosensitizers [Re(Cl)(CO)$_3$(N,N)] and [Re(imidazole)(CO)$_3$(N,N)]$^+$: Diimine Effects. *Inorg. Chem.* **2011,** *50*, 2932–2943.
69. Harabuchi, Y.; Eng, J.; Gindensperger, E.; Taketsugu, T.; Maeda, S.; Daniel, C., Exploring the Mechanism of Ultrafast Intersystem Crossing in Rhenium(I) Carbonyl Bipyridine Halide Complexes: Key Vibrational Modes and Spin−Vibronic Quantum Dynamics. *J. Chem. Theory Comput.* **2016,** *12*, 2335−2345.

Table of contents graphics